ARTICLE OPEN

Check for updates

Coupling of radiation and grain boundary corrosion in SiC

Jianqi Xi [1,5✉], Hongliang Zhang[2,5✉], Ranran Su[3], Shuguang Wei[1], Xuanxin Hu[1], Benoit Queylat[4], Taeho Kim[4], Adrien Couet [1,4] and Izabela Szlufarska[1,4✉]

Radiation and corrosion can be coupled to each other in non-trivial ways and such coupling is of critical importance for the performance of materials in extreme environments. However, it has been rarely studied in ceramics and therefore it is not well understood to what extent these two phenomena are coupled and by what mechanisms. Here, we discover that radiation-induced chemical changes at grain boundaries of ceramics can have a significant (and positive) impact on the corrosion resistance of these materials. Specifically, we demonstrate using a combination of experimental and simulation studies that segregation of C to grain boundaries of silicon carbide leads to improved corrosion resistance. Our results imply that tunning of stoichiometry at grain boundaries either through the sample preparation process or via radiation-induced segregation can provide an effective method for suppressing surface corrosion.

INTRODUCTION

The fast-growing energy demand and the need to limit greenhouse gas emissions have led to the acknowledgment of the importance of increasing energy efficiency, which requires materials that can withstand more and more extreme environments. For example, the advances in nuclear reactors create exceptionally harsh working conditions for materials operating at higher temperatures, and more intensive radiation doses, while maintaining integrity in the presence of chemically aggressive environments[1–5]. In some cases, the effects of these environments can even couple with each other[2–4]. Those challenging environments can degrade materials' performance, thus calling for fundamental improvement in materials. Ceramics are excellent candidates for such extreme environments due to their high-temperature mechanical stability and chemical stability[6–10]. However, while studies of radiation effects in metals have been quite extensive, much less is known about radiation effects in ceramics and especially how they are coupled to corrosion resistance[6,7].

Examples of the coupled effects of extreme environments in metals include stress corrosion cracking and the impact of radiation-induced local chemical changes on corrosion[1–4,11–18]. The evolution of local chemical changes in metals under irradiation has an interesting effect on corrosion resistance and can even decrease the oxidation rate of materials[16,17]. Unlike metals, ceramics have much more complex energy landscapes for radiation defect reactions and multiple sublattices in which defects can migrate. This defect behavior makes the radiation resistance of ceramics complicated and interesting at the same time. In particular, radiation-induced local chemical changes at interfaces, e.g., radiation-induced segregation (RIS) in ceramics have been discovered only recently in SiC[19], and the underlying fundamental mechanisms are very different from those in metals. Specifically, RIS in ceramic can occur at a much lower irradiation temperature than typical RIS in metallic systems (between $0.3T_m$ and $0.5T_m$[20]). This phenomenon in ceramics is related to the energy barriers for defect recombination and to the chemically unbalanced diffusion of species to surfaces along grain boundaries (GBs).

In ceramics, there is some evidence that radiation may impact corrosion resistance, but the reasons for this coupling effect are still unknown. For example, a recent experimental study reported radiation-enhanced corrosion of polycrystalline SiC[21]. However, it is unclear if the accelerated corrosion is due to the radiation-induced chemical changes at GB itself or due to the radiolysis of the coolant water. An important fundamental question with a significant potential impact on applications is related to the role that radiation-induced chemical changes in grain boundaries of ceramics play in corrosion resistance. A significant coupling between RIS and corrosion would suggest that extensive studies of RIS in ceramics are necessary for these materials to be reliable in radiation environments.

Here, we discover that radiation-induced chemical changes in ceramics lead to significant changes in corrosion resistance. Using a combination of experimental and simulation methods, we also demonstrate that it is possible for RIS to decelerate corrosion in ceramics, suggesting a beneficial effect of RIS in selected environments. SiC is selected as a model ceramic, but also one that is highly promising for advanced nuclear reactors.

RESULTS AND DISCUSSION

Radiation-induced segregation in bicrystal SiC

Radiation-induced segregation (RIS) was previously discovered at GBs of SiC at an irradiation dose of ~1 displacement per atom (dpa)[19]. It was also found that RIS is more pronounced at high-angle GBs (HAGBs)[19]. In order to investigate the effect of RIS on the corrosion resistance of SiC, here we synthesized a number of SiC bicrystals for irradiation experiments (with hexagonal 4H crystal structure). The detailed information about the synthesis and characterization of the SiC bicrystals can be found in the Supplementary Materials. The samples were irradiated with 6.0 MeV Si ions with a fluence of 7.5×10^{16} ions cm^{-2} at 300 °C, which generated an average damage dose of 3 dpa within 1.8 μm of the sample surface based on the Stopping and Range of Ions in Matter (SRIM)[22] calculations. We confirmed the presence of RIS in

---

[1]Department of Materials Science & Engineering, University of Wisconsin–Madison, Madison, WI, USA. [2]Institute of Modern Physics, Fudan University, Shanghai, China. [3]School of Nuclear Science and Engineering, Shanghai Jiao Tong University, Shanghai, China. [4]Department of Engineering Physics, University of Wisconsin–Madison, Madison, WI, USA. [5]These authors contributed equally: Jianqi Xi, Hongliang Zhang. ✉email: jianqixi@illinois.edu; hlz@fudan.edu.cn; szlufarska@wisc.edu
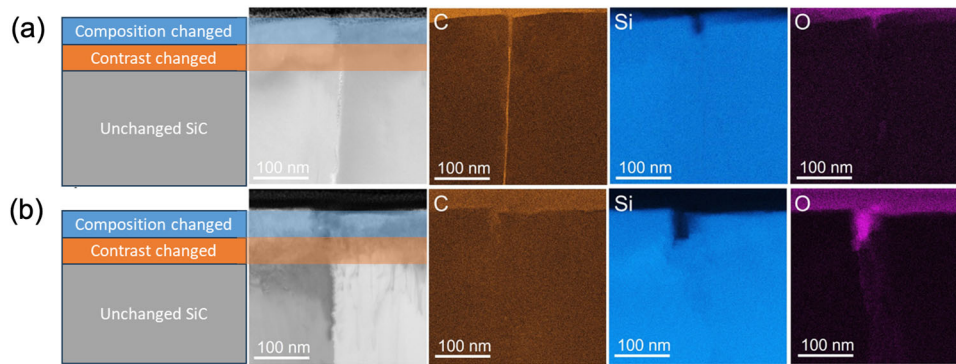
Fig. 1 STEM and EDS mapping of SiC bicrystal (30° twist, 5.6° tilt) corroded in an autoclave in flowed, pure, deaerated, and deionized water (18 MΩ resistivity) at 360 °C for 30 days. a Sample irradiated at 300 °C to the dose of 3 dpa and **b** non-irradiated sample. Note that the thickness of the corroded layer at GBs in both samples is <100 nm, indicating that the EDS distribution in the deep region of the samples would not be affected by the hydrothermal corrosion.

our samples using a combination of scanning transmission electron microscopy (STEM) and energy-dispersive X-ray spectroscopy (EDS) mapping. In the following, we present the results based on the bicrystal with misorientation of 30° twist and 5.6° tilt as a representative example of HAGB (see Fig. 1). Figure 1 shows that the concentration of C at the GB in the irradiated sample is higher than in the non-irradiated sample, confirming the presence of RIS in our bicrystal samples. We investigated 3 unirradiated samples, 3 samples irradiated at 300 °C for 3 dpa for this specific bicrystal misorientation, using an EDS line scan and map scan. All of them showed qualitatively the same trend. It should be noted that the samples shown in Fig. 1 were obtained after the hydrothermal corrosion test at 360 °C for 30 days. The experimental conditions for the autoclave are described in the "Methods" section of this paper. According to previous experiments and simulations[21,23], hydrothermal corrosion occurs through the dissolution of Si from SiC. Our experimental results, backed by STEM-EDS and TEM analyses, reveal two distinct layers that formed after corrosion, as shown in Fig. 1. Layer 1 (near the surface, thickness of ~100 nm): This layer exhibits changes in both chemical composition and diffraction contrast. Layer 2 (depth beyond ~100 nm): Here, although the chemical composition remains unchanged, the diffraction contrast varies. This contrast alteration is likely due to strain that arises from microstructural differences and lattice mismatch between the oxide layer and SiC. We define the corroded layer as Layer 1, where both the chemical composition and the diffraction contrast have altered. In Fig. 1, we observe that the thickness of the corroded layer at GBs in both samples is <100 nm, suggesting that the deep region of the samples would not be affected by hydrothermal corrosion. Therefore, the relative carbon enrichment in the irradiated sample should be attributed to RIS rather than the dissolution of Si species during corrosion.

RIS decelerates the intergranular corrosion of bicrystal SiC

Both irradiated and non-irradiated bicrystal samples were subjected to a pure water corrosion test in an autoclave at 360 °C under 18.0 MPa. The samples were analyzed by weight change measurements (see Supplementary Materials), scanning electron microscope (SEM), and TEM to study the overall corrosion rate as well as surface morphology and microstructural changes induced by corrosion. In general, for the surface region that is far away from the GB, the corrosion rates in both irradiated and non-irradiated SiC samples are comparable, i.e., the corroded layer has a comparable thickness in both samples (see Supplementary Table 2). However, there are significant differences in the corroded samples closer to the GB regions. An example is shown in Fig. 2. The thickness of the corroded layer in the non-irradiated sample,

~60 nm, is much larger than that in the irradiated sample, ~22 nm, providing evidence that radiation can decrease the intergranular corrosion rate of SiC. Figure 2c and d show the depth-resolved concentration profiles in the samples. One can see there is a C depletion region at the GB deeper in the non-irradiated sample (Fig. 2c), which is a common phenomenon in as synthesized SiC GBs[19]. In contrast, in the irradiated sample, the GBs are enriched in C enrichment due to RIS (Fig. 2d). These profiles also show that within the corroded layer, the atomic percentage of Si is dramatically decreased, whereas the percentages of C and O are increased. To further validate our findings that the corrosion rate of GB regions in irradiated samples is lower than that of unirradiated samples, we conducted EDS line scans on 10 TEM foils extracted from unirradiated and irradiated samples for the corrosion condition of 360 °C, 30 days. Detailed information about more corrosion conditions and TEM samples is shown in the "Methods" section. Detailed results of this investigation can be found in Supplementary Table 3. These results are consistent with earlier corrosion studies[23,24], where surface corrosion was found to occur by the dissolution of Si into the surrounding water.

To exclude the possibility that the thinner corroded layer observed on the irradiated sample is the result of SiC having dissolved into the water during corrosion, we used FIB to lift out a sample at the boundary between non-irradiated and irradiated regions, and the lift-out sample includes both regions. TEM analysis of the sample revealed no step on the surface across the boundary between the regions, confirming that the difference in thickness of the corroded layers is not due to more material being dissolved on the unirradiated side of the sample, but instead to a larger penetration of the corrosion front into the bulk. We have also checked the distance from the surface to the peak of the ion implantation before and after corrosion. TEM analysis showed that the thickness of the irradiated region (the distance from the surface to the inner edge of the damage peak) is the same (2.98 μm) in both samples and that it does not change during corrosion, providing further evidence that the dissolution of SiC is negligible. Therefore, the thinner corroded layer in the GB region of the irradiated samples as compared to non-irradiated samples can be attributed to a lower corrosion rate.

Radiation-decelerated corrosion in metal alloys has been successfully explained on the basis of the radiation-enhanced diffusion of defects[11,12]. Diffusion can accelerate reactions between the metal and the dissociated oxygen resulting in a faster formation of a protective oxide layer on the surface during irradiation[11]. This explanation does not apply to the case of SiC, because SiC does not form a protective oxide layer in high-temperature water. Instead, it forms a thin SiCO layer that is eventually dissolved into water as silicic acid and carbon gas phases[23].
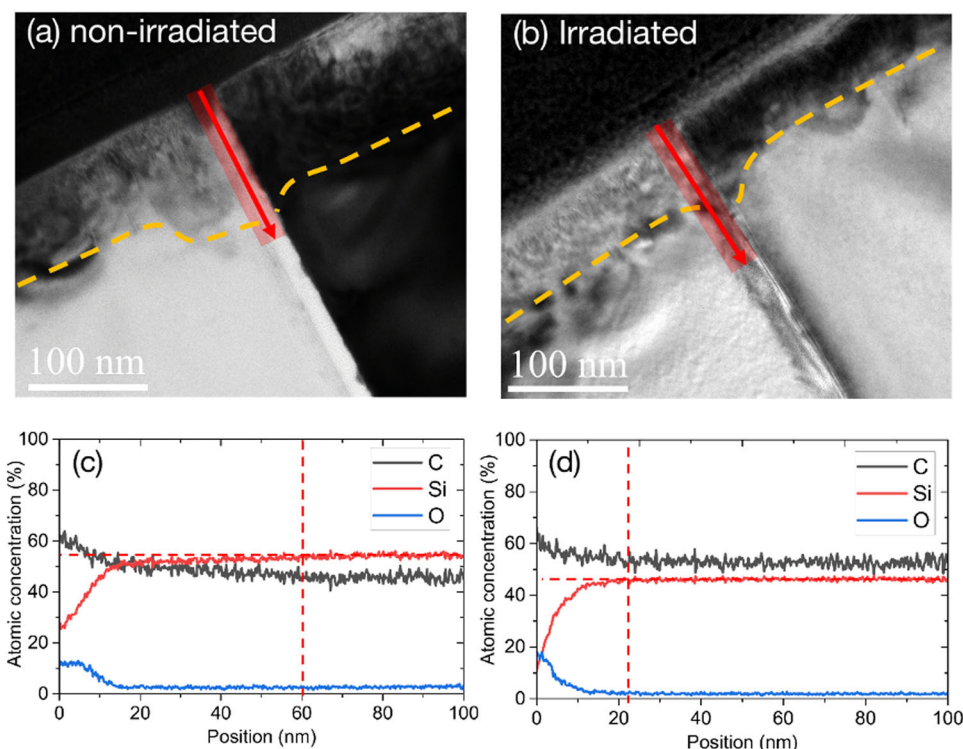
Fig. 2 TEM images and EDS spectra of the corroded bicrystal SiC at 360 °C for 30 days in pure water without and with irradiation. a and **b** are the TEM images of the corroded samples without and with irradiation, respectively. The corresponding atomic percentages of Si, C, and O, determined from the EDS, as a function of distance from the surface along the GB region are shown in (**c**) and (**d**), respectively. The horizontal dash lines in (**c**) and (**d**) show the value of the atomic percentage of Si species at the GB deeper in the sample, and the vertical dash lines identify the depth that the atomic percentage of Si species begins to reduce due to corrosion.

To clarify the radiation-decelerated corrosion in SiC, we have performed atomistic simulations to study the corrosion of SiC bicrystals with different stoichiometries. Based on our earlier simulation studies[23,24], the corrosion mechanism at the GB is related to hydrogen scission reactions. Specifically, as the water molecules dissociate near the surface, most of the hydrogen can penetrate along the GB. Hydrogen breaks the Si-C bonds, it bonds preferentially to C, and Si is released into the water as $Si(OH)_4$[23,24]. Therefore, the corrosion rate is determined by the dissolution rate of Si species from samples as well as the surface Si–C bonds of the samples, as shown in Fig. 3. In the comparison of the dissolution rate of Si species from samples with different stoichiometries, we calculated the normalized number of dissolved Si atoms at GB regions (see Fig. 3a). Normalization means that we divided the number of dissolved Si atoms from the GB by the total number of Si atoms in the GB. Figure 3 shows that the Si dissolution rate of the C-rich GB is generally smaller than the dissolution rates of the stoichiometric and the Si-rich GBs. The changes in Si–C surface bonds have further confirmed these results, as shown in Fig. 3b. It is known that the environmental degradation of SiC in high-temperature water is accomplished by the breaking of Si–C surface bonds by H (referred to as hydrogen scission reaction)[23,24]. Here, we have quantified the changes in the number of surface Si–C bonds in SiC GBs (see Fig. 3b). We found that the number of surface Si–C bonds at the Si-rich GB region is reduced by ~25% over the 600 ps of the simulation time, while at the C-rich GB region, it is only reduced by ~9%. The above results demonstrate that the C enrichment at GBs can decelerate the degradation of SiC. It should be noted that the depth of the corroded C-rich sample is around 1 nm in the MD simulation time scale, and the corresponding corrosion rate in the MD simulation is in the order of ~10^8 nm^2 s^{-1}, which is much larger than that in the experimental measurements, ~10^{-1} nm^2 s^{-1}. This difference could

be either from the temperature difference that the MD simulation was performed at a higher temperature compared with the experimental conditions or from the composition difference in the simulation and experimental samples, etc. Even though the corrosion rate in simulation is quantitatively faster than that in experiments, both the simulations and experiments show the deceleration of corrosion as the C contents increased.

Based on our simulations, there are two possible reasons for the radiation-decelerated corrosion in SiC GBs. First, the radiation-induced C segregation at GBs can create many C–C bonds, and due to the preferential interaction between C and H, those C–C bonds can attract H atoms to form the C–H bonds. This selective attraction will mitigate the hydrogen scission of the Si–C surface bonds. This is evident in Fig. 3c, where the number of H atoms interacting with the C–C bonds at the C-rich GB is much larger than that at the Si-rich GB. Secondly, according to our earlier quantum mechanical calculations[25], the stiffness of the underlying solid can also play a significant role in controlling surface corrosion reactions. Specifically, surface reactions cause elastic relaxation of the surrounding solid, and consequently, there is a release of the stored mechanical energy induced by the surface reaction. For materials with lower stiffness, the amount of elastic energy released is higher, leading to a reduction in the reaction energy[26]. The calculated bulk moduli of the model bicrystals with different stoichiometries are 148.36 GPa for a stoichiometric GB, 149.34 GPa for Si-rich GB, and 153.73 GPa for C-rich GB. The higher modulus of a bicrystal with a C-rich boundary is consistent with the slower surface corrosion reaction in the C-rich GB.

In summary, understanding the coupled effects of radiation and corrosion in materials provides the necessary foundation to explain and predict the performance of materials for applications in extreme environments, especially for materials in nuclear applications. We have shown that the radiation-induced chemical
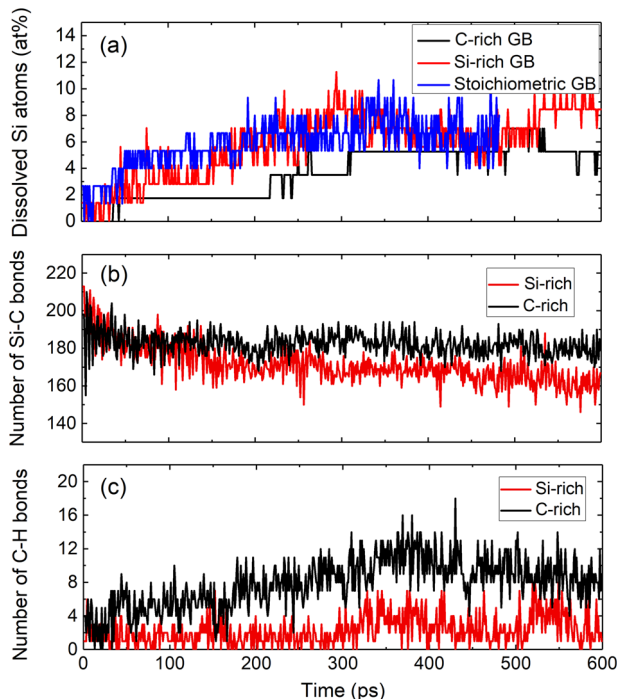
Fig. 3 The simulated intergranular corrosion of SiC at different stoichiometric conditions. a Normalized dissolved Si atoms in SiC GB regions with different stoichiometries. Normalization here means the ratio of the number of dissolved Si atoms from the GB to the total number of Si atoms in the GB region. **b** The number of Si–C bonds in the C-rich and Si-rich SiC GBs. **c** The number of H atoms binding with the C–C bonds in the C-rich and Si-rich SiC GB region. All the results are from MD simulations and they are averaged over two independent simulations with different distributions of excess C atoms.

changes in GBs couple to the corrosion resistance of ceramics, using SiC as a model covalent material as well as a material of great interest for applications in radiation environments. Our results reveal that radiation can decelerate intergranular corrosion through radiation-induced segregation of C to GBs of SiC. Specifically, the local chemical changes can modify chemical reactivity by modifying interactions with H atoms from dissociated water and by increasing local stiffness. The impact of RIS on corrosion resistance will depend on the environment. In our hydrothermal corrosion experiments, there was no oxygen dissolved in the water. Had the oxygen been present, the corrosion reaction could have been changed by oxidation, and the corrosion rate might have been accelerated by radiation as shown in the previous studies[27,28]. Our discovery of the coupling between radiation and corrosion in ceramics suggests the possibility of engineering GB stoichiometries such that the evolution of GB under non-equilibrium conditions of nuclear reactors increases their corrosion resistance. The stoichiometry of materials can be controlled either in the sample preparation process or via RIS. The mechanisms of how radiation is coupled to corrosion in the absence of a stable oxide layer are distinct from what has been reported so far for metallic systems.

METHODS

Bicrystal SiC sample fabrication

The SiC bicrystals were fabricated following the procedure outlined below. First, 4H-SiC single crystal wafers were cut using a diamond pen according to the desired GB misorientation angles. Second, chemical cleaning was conducted on the wafers to

remove possible contaminations and oxidation layers. This procedure starts with cleaning using piranha solution (H_2SO_4 and H_2O_2 with 4:1 mixture) at 180 °C for 20 min, followed by deionized water cleaning for 5 min. The wafers were then cleaned in HF (~40%) at room temperature for 2 h, followed by deionized water cleaning for 5 min. After that, the wafers were cleaned with a solution prepared with a 4:1:1 mixture of H_2O, H_2O_2, and HCl at 80 °C for 15 min, followed by deionized water washing for 5 min. The wafers were then cleaned in dilute HF (5%) at room temperature for 15 min, followed by deionized water cleaning for 10 min. Thirdly, hydrogenation was performed to make sure the wafer surface was free of oxidation. The cleaned wafers were put into a tube furnace and annealed in pure hydrogen (99.99%) at 0.1 MPa, 1000 °C for 2 h. Finally, the wafers, after hydrogenation, were put into graphite dies and transferred to a hot-pressing furnace for bonding. The bonding temperature was 1000 °C, the bonding pressure was 30 MPa, and the bonding time was 20 h. The misorientations of the SiC bicrystals were designed to be 30° twist and 5.6° tilt (high angle), 15° twist and 0° tilt (medium angle), and 10° twist and 0° tilt (low angle). Hydrogenation is a common process in the semiconductor industry for oxide layer removal. Typically, the industry standard for annealing to remove surface hydrogen ranges between 400 and 600 °C for a duration of 2–4 h. Under these conditions, the hydrogen is fully desorbed from the surface. In our bonding processing, we go beyond these standards by annealing the SiC samples at 1000 °C for 24 h. This process ensures that any residual hydrogen is effectively removed, thus eliminating the possibility of hydrogen retention.

The morphology and misorientations of the fabricated bicrystals were analyzed by SEM and transmission electron backscatter diffraction (tEBSD) mapping. The samples were imaged using an FEI Helios PFIB G4 FIB/FESEM system, and then the same foil was transferred to an FEI Titan to acquire a bright field (BF)-transmission electron microscopy (TEM) image. By comparing the tEBSD mapping and the contrast in BF-TEM images, we could identify the locations and misorientations of the GBs shown in the BF-TEM images. GBs that could be tilted to edge-on conditions were selected for the following FIB milling and TEM analyses.

According to tEBSD mapping, the GB twist angle is 28°, and the tilt angle is 5.6°, which are close to the designed values (30° twist and 5.6° tilt). We note that some regions along the GBs are not tightly bonded, especially near the edge and surface of the bonded wafers. The loosely bonded regions appear as cracks that are about tens or hundreds of nanometers in length along the GB. TEM analyses were performed in regions far away from these cracks (typically around 10 μm from the cracks).

Radiation experiments and damage profile calculation

The bicrystal SiC and CVD SiC were irradiated by 6.0 MeV Si ions with an irradiation fluence of 7.78×10^{16} ions cm^{-2}, a flux of 9.0×10^{11} ions cm^{-2} s, and an irradiation temperature of 300 and 600 °C. The total irradiation time was 18 h. The irradiation was parallel to the GB normal. The radiation damage profile of 6.0 MeV Si ions in SiC is calculated using SRIM-2013[22], using the quick Kinchin–Pease Mode, assuming the displacement threshold energy is 35 eV for silicon and 20 eV for carbon. The density of 3C-SiC and 4H-SiC used for the calculation is 3.1 g cm^{-3}. Supplementary Fig. 2 corresponds to the damage profile of the irradiation with 6.0 MeV Si ions with a fluence of 7.78×10^{16} ions cm^{-2}.

Corrosion experiments

Both the bicrystal SiC and CVD SiC samples were corroded in flowed, pure, deaerated, and deionized water (18 MΩ resistivity), in an autoclave at 360 °C, 18 MPa. No additional hydrogen was added. No additional chemical control was applied. Prior to, and following each corrosion in an autoclave, inductively coupled plasma-optical emission spectrometry (ICP-OES) was used to measure the trace
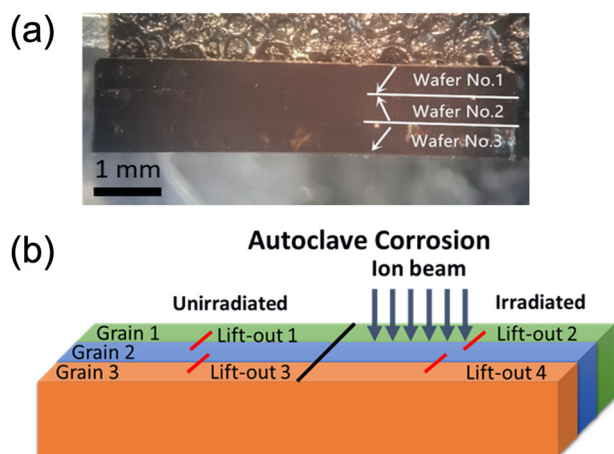
Fig. 4 The synthesized SiC bicrystal samples for ion irradiation and autoclave corrosion. a Photograph of the synthesized SiC bicrystals. Wafer Nos. 1–3 are the three SiC grains with different orientations, and arrows schematically show the grain orientation and **b** Schematic representation of the bicrystals illustrating sample details and the locations for lift-out. Different colors denote the grains with different orientations.

element concentrations present in the pure deaerated water to ensure oxidizing conditions below a pH of 8.00. The pH calculations were completed using ChemWorks MULTEQ® Software Version 4.1. The corrosion time is 7, 15, and 30 days. The oxygen content in the autoclave was on the order of 1.0 ppm. For each corrosion condition, we corroded a total of 8 bulk bicrystal samples with different misorientations. Half of each bicrystals were unirradiated, while the other half was irradiated. This procedure ensured that we compared unirradiated and irradiated bicrystals with the same misorientations, as shown in Fig. 4. Furthermore, to eliminate any potential variations in the environment or synthesis method, we performed controlled experiments using the CVD SiC samples. These CVD SiC samples were corroded simultaneously with the bicrystals within the same autoclave.

TEM sample preparation

Samples for the TEM analysis were prepared using a standard lift-out technique by an FEI Helios PFIB G4 FIB/FESEM Focused Ion Beam (FIB) instrument in the Materials Science Center at the University of Wisconsin-Madison. To protect the sample surface from damage during the sample preparation, a 3.0 μm Pt protective layer was deposited on the surface in two steps: (i) 2 kV electron beam (low energy) was used to deposit a 1.0 μm Pt layer to avoid damage from high-energy ions deposition; (ii) a 12 kV ion beam was used for the deposition of another 2.0 μm Pt layer. The thinning process was sped up by a high-energy ion beam (30 kV) at the beginning and ended with a low-energy ion beam (2 kV) to carefully remove the amorphous area generated in the former stage. The amorphous layer generated in the former stage was finally removed by an 800 V ion beam from Fischione's Model 1040 NanoMill. We prepared multiple TEM foils for each individual sample. For instance, for the corrosion condition of 360 °C for 30 days, we prepared 3 TEM foil samples from an unirradiated bicrystal with a misorientation of 30° twist and 5.6° tilt, as well as 3 TEM foil samples from a 300 °C, 3 dpa irradiated bicrystal with the same misorientation. Additionally, we prepared 2 TEM foil samples from an unirradiated bicrystal with a misorientation of 15° twist and 5.6° tilt, along with 2 TEM foil samples from a 300 °C, 3 dpa irradiated bicrystal with the same misorientation. Thus, we examined a total of 10 TEM foil samples with different misorientations under this particular corrosion condition. Moreover, we also examined multiple TEM foils from

chemical vapor deposition (CVD) SiC samples that were corroded at different conditions, both with and without irradiation, to further validate our results.

Experimental TEM and STEM EDS spectrum image data acquisition

FEI Tecnai F30 with field emission gun (FEG) TEM was used to analyze the damage and the microstructure before and after irradiation. Detailed structural and chemical analysis of the SiC samples was carried out using high-angle annular dark-field scanning transmission electron microscopy (HAADF-STEM) images and energy dispersive X-Ray spectroscopy (EDS) in an FEI Titan G2 80–200 (S)TEM equipped with the Super-X EDS detection system. The microscope was operated at an acceleration voltage of 200 kV, with a probe current of approximately 300 pA and a probe convergence angle of 21 mrad. Simultaneous HAADF and EDS acquisitions were performed using the Bruker Esprit software. All the line and map scans were obtained with a step size of 0.3 nm, and a dwell time of 20 s with a spot size of 6 to get a stronger signal and good statistics. The total scan region was sized in 100 nm for the line scan and 500 nm × 500 nm for the map scan. A drift-corrected spectrum was acquired over 100 frames, with a 50 μs per pixel dwell time and a 30 s interval between applications of drift correction using the acquired HAADF image. As the counting rate of the EDS signals is also sensitive to the thickness of the samples, the thickness of the samples was measured by electron energy-loss spectroscopy (EELS). The results show that the thickness of all the measured regions is around 80 nm.

Molecular dynamics simulations

The hydrothermal corrosion was carried out in the MD simulations using reactive force field ReaxFF[29], as implemented in the large-scale atomic/molecular massively parallel simulator (LAMMPS) package[26]. We have previously tested different versions of the ReaxFF force fields[29–31] and found the parameters developed by Yeon et al.[29] can predict the water density and the hydroxylation reaction for Si–O structures in the best agreement with our ab initio MD simulations and DFT calculations[23,24]. Considering the dominance of incoherent GBs in engineered 3C–SiC and the fact that they provide fast corrosion pathways, in this study, we perform simulations on bicrystals with incoherent GBs. The model of bicrystal SiC was built by combining two single crystals with different crystallographic orientations. The dimensions parallel to the grain boundary are around 32 and 60 Å, and the thickness of the sample is around 60 Å. The dimension perpendicular to the grain boundary is around 126 Å. The details of the modeling of bicrystal have been discussed elsewhere[32,33]. Above the sample, a vacuum region with 32 Å × 40 Å × 126 Å has been created. To prepare a model of the water environment, we first created a cell (the cell size is the same as the vacuum region) containing 1300 water molecules, corresponding to a water density of 0.24 g cm^{-3}. Positions of water molecules were random and were first chosen using the Packmol code[34]. Subsequently, we relaxed the system for 100 ps at 1000 K with the time step of 0.25 fs and the use of periodic boundary conditions in all the spatial directions. The temperature was controlled using the Nose–Hoover thermostat. After relaxation, we inserted these water molecules into the vacuum region above bicrystal SiC surface, equilibrated the entire system, and then performed simulations at 1000 K to simulate the hydrothermal corrosion process for 600 ps. To determine the role of stoichiometry in intergranular corrosion, we considered three SiC bicrystals with different stoichiometric conditions, corresponding to the Si-rich grain boundary, stoichiometric grain boundary, and C-rich grain boundary. Specifically, around 10% of antisite defects were uniformly and randomly distributed within 10 Å-thick regions centered at each incoherent GB. We considered two different random distributions for the MD simulations and averaged the final results in the analysis.

The elastic modulus of bicrystal with different stoichiometric conditions was performed using the Vashishta potential[35]. The elastic properties for bicrystal SiC were calculated from stress–strain curves. The relationship between stress and strain is described according to Hooke's law as $\sigma_{ij} = \sum_{k=1}^{3} \sum_{l=1}^{3} C_{ijkl}\varepsilon_{kl}$, where σ_{ij} is the stress, ε_{kl} is the strain, and C_{ijkl} is the stiffness constant tensor. The elastic moduli can be derived by calculating the components of the stiffness constant tensor.

DATA AVAILABILITY
All data that support the findings of this study are involved in this Main text and the Supplementary Information.

REFERENCES
1. Was, G. S., Petti, D., Ukai, S. & Zinkle, S. Materials for future nuclear energy systems. *J. Nucl. Mater.* **527**, 151837 (2019).
2. Bruemmer, S. M. et al. Radiation-induced material changes and susceptibility to intergranular failure of light-water-reactor core internals. *J. Nucl. Mater.* **274**, 299–314 (1999).
3. Allen, T., Busby, J., Meyer, M. & Petti, D. Materials challenges for nuclear systems. *Mater. Today* **13**, 14–23 (2010).
4. Zinkle, S. J. & Was, G. S. Materials challenges in nuclear energy. *Acta Mater.* **61**, 735–758 (2013).
5. Zhang, H. et al. The damage evolution of He irradiation on Ti$_3$SiC$_2$ as a function of annealing temperature. *J. Eur. Ceram. Soc.* **38**, 1253–1264 (2018).
6. Lee, W. E., Gilbert, M., Murphy, S. T. & Grimes, R. W. Opportunities for advanced ceramics and composites in the nuclear sector. *J. Am. Ceram. Soc.* **96**, 2005–2030 (2013).
7. Marra, J. Advanced ceramic materials for next-generation nuclear applications. *IOP Conf. Ser. Mater. Sci. Eng.* **18**, 162001 (2011).
8. Bongiorno, A. et al. A perspective on modeling materials in extreme environments: Oxidation of ultrahigh-temperature ceramics. *MRS Bull.* **31**, 410–417 (2006).
9. Su, R. et al. Enhanced oxidation resistance of (Mo95W5)85Ta10(TiZr)5 refractory multi-principal element alloy up to 1300 °C. *Acta Mater.* **215**, 117114 (2021).
10. Zhang, H. et al. Enhancing the phase stability of ceramics under radiation via multilayer engineering. *Sci. Adv.* **7**, eabg7678 (2021).
11. Tan, L., Allen, T. R. & Busby, J. T. Grain boundary engineering for structure materials of nuclear reactors. *J. Nucl. Mater.* **441**, 661–666 (2013).
12. Asher, R. C., Davies, D., Kirstein, T. B. A., McCullen, P. A. J. & White, J. F. The effects of radiation on the corrosion of some Zr alloys. *Corros. Sci.* **10**, 695–707 (1970).
13. He, M. R., Johnson, D. C., Was, G. S. & Robertson, I. M. The role of grain boundary microchemistry in irradiation-assisted stress corrosion cracking of a Fe–13Cr–15Ni alloy. *Acta Mater.* **138**, 61–71 (2017).
14. Raiman, S. S. & Was, G. S. Accelerated corrosion and oxide dissolution in 316L stainless steel irradiated in situ in high temperature water. *J. Nucl. Mater.* **493**, 207–218 (2017).
15. Zhang, H. et al. Nano-porosity effects on corrosion rate of Zr alloys using nanoscale microscopy coupled to machine learning. *Corros. Sci.* **208**, 110660 (2022).
16. Hanbury, R. D. & Was, G. S. Oxide growth and dissolution on 316L stainless steel during irradiation in high temperature water. *Corros. Sci.* **157**, 305–311 (2019).
17. Zhou, W. et al. Proton irradiation-decelerated intergranular corrosion of Ni–Cr alloys in molten salt. *Nat. Commun.* **11**, 3430 (2020).
18. Schmidt, F. et al. Effects of radiation-induced defects on corrosion. *Annu. Rev. Mater. Res.* **51**, 293–328 (2021).
19. Wang, X. et al. Radiation-induced segregation in a ceramic. *Nat. Mater.* **19**, 992–998 (2020).
20. Was, G. S. et al. Assessment of radiation-induced segregation mechanisms in austenitic and ferritic-martensitic alloys. *J. Nucl. Mater.* **411**, 41–50 (2011).
21. Doyle, P. et al. The effects of neutron and ionizing irradiation on the aqueous corrosion of SiC. *J. Nucl. Mater.* **536**, 152190 (2020).
22. Stoller, R. E. et al. On the use of SRIM for computing radiation damage exposure. *Nucl. Instrum. Methods Phys. Res. Sect. B* **310**, 75–80 (2013).
23. Xi, J., Liu, C., Morgan, D. & Szlufarska, I. Deciphering water-solid reactions during hydrothermal corrosion of SiC. *Acta Mater.* **209**, 116803 (2021).
24. Xi, J., Liu, C., Morgan, D. & Szlufarska, I. An Unexpected Role of H during SiC Corrosion in Water. *J. Phys. Chem. C* **124**, 9394–9400 (2020).
25. Xi, J. & Szlufarska, I. Control of surface chemical reactions through solid stiffness. *Phys. Rev. Lett.* **129**, 106101 (2022).
26. Plimpton, S. Fast parallel algorithms for short-range molecular dynamics. *J. Comput. Phys.* **117**, 1–19 (1995).
27. Shin, J. H., Kim, D., Lee, H. G., Park, J. Y. & Kim, W. J. Factors affecting the hydrothermal corrosion behavior of chemically vapor deposited silicon carbides. *J. Nucl. Mater.* **518**, 350–356 (2019).
28. Kondo, S., Lee, M., Hinoki, T., Hyodo, Y. & Kano, F. Effect of irradiation damage on hydrothermal corrosion of SiC. *J. Nucl. Mater.* **464**, 36–42 (2015).
29. Yeon, J. & Van Duin, A. C. T. ReaxFF molecular dynamics simulations of hydroxylation kinetics for amorphous and nano-silica structure, and its relations with atomic strain energy. *J. Phys. Chem. C* **120**, 305–317 (2016).
30. Fogarty, J. C., Aktulga, H. M., Grama, A. Y., Van Duin, A. C. T. & Pandit, S. A. A reactive molecular dynamics simulation of the silica-water interface. *J. Chem. Phys.* **132**, 174704 (2010).
31. Newsome, D. A., Sengupta, D., Foroutan, H., Russo, M. F. & Van Duin, A. C. T. Oxidation of Silicon Carbide by O$_2$ and H$_2$O: A ReaxFF Reactive Molecular Dynamics Study, Part I. *J. Phys. Chem. C* **116**, 16111–16121 (2012).
32. Liu, C., Xi, J. & Szlufarska, I. Sensitivity of SiC grain boundaries to oxidation. *J. Phys. Chem. C* **123**, 11546–11554 (2019).
33. Xi, J., Liu, C. & Szlufarska, I. Effects of point defects on oxidation of 3C–SiC. *J. Nucl. Mater.* **538**, 152308 (2020).
34. Allouche, A. Software news and updates gabedit—a graphical user interface for computational chemistry softwares. *J. Comput. Chem.* **32**, 174–182 (2012).
35. Vashishta, P., Kalia, R. K., Nakano, A. & Rino, J. P. Interaction potential for silicon carbide: a molecular dynamics study of elastic constants and vibrational density of states for crystalline and amorphous silicon carbide. *J. Appl. Phys.* **101**, 103515 (2007).

AUTHOR CONTRIBUTIONS
J.X., H.Z. and I.S.: conceptualization and methodology, manuscript writing, review and editing, formal analysis; H.Z.: sample preparation and radiation experiments; H.Z., R.S., S.W., H.X.: experimental characterization work; H.Z., B.Q., T.K.: corrosion experimental work; A.C.: manuscript review and editing.

COMPETING INTERESTS
The authors declare no competing interests.

ADDITIONAL INFORMATION
Supplementary information The online version contains supplementary material available at https://doi.org/10.1038/s41529-024-00436-y.

Correspondence and requests for materials should be addressed to Jianqi Xi, Hongliang Zhang or Izabela Szlufarska.

Reprints and permission information is available at http://www.nature.com/reprints

Publisher's note Springer Nature remains neutral with regard to jurisdictional claims in published maps and institutional affiliations.